LANGMUIR Article
Cite This: Langmuir 2019, 35, 7659−7671
pubs.acs.org/Langmuir

Dynamics of Liquid Transfer from Nanoporous Stamps in High-Resolution Flexographic Printing

Dhanushkodi D. Mariappan,[†] Sanha Kim,[†] Michael S. H. Boutilier,[†] Junjie Zhao,[‡] Hangbo Zhao,[†] Justin Beroz,[†] Ulrich Muecke,[⊥] Hossein Sojoudi,[‡] Karen Gleason,[‡] Pierre-Thomas Brun,[∥,§] and A. John Hart*[,†]

[†]Department of Mechanical Engineering, [‡]Department of Chemical Engineering, [§]Department of Mathematics, [⊥]Department of Materials Science and Engineering, Massachusetts Institute of Technology, Cambridge, Massachusetts 02139, United States
[∥]Department of Chemical and Biological Engineering, Princeton University, Princeton, New Jersey 08544, United States

Supporting Information

ABSTRACT: Printing of ultrathin layers of polymeric and colloidal inks is critical for the manufacturing of electronics on nonconventional substrates such as paper and polymer films. Recently, we found that nanoporous stamps overcome key limitations of traditional polymer stamps in flexographic printing, namely, enabling the printing of ultrathin nanoparticle films with micron-scale lateral precision. Here, we study the dynamics of liquid transfer between nanoporous stamps and solid substrates. The stamps comprise forests of polymer-coated carbon nanotubes, and the surface mechanics and wettability of the stamps are engineered to imbibe colloidal inks and transfer the ink upon contact with the target substrate. By high-speed imaging during printing, we observe the dynamics of liquid spreading, which is mediated by progressing contact between the nanostructured stamp surface and by the substrate and imbibition within the stamp−substrate gap. From the final contact area, the volume of ink transfer is mediated by rupture of a capillary bridge; and, after rupture, liquid spreads to fill the area defined by a precursor film matching the stamp geometry with high precision. Via modeling of the liquid dynamics, and comparison with data, we elucidate the scale- and rate-limiting aspects of the process. Specifically, we find that the printed ink volume and resulting layer thickness are independent of contact pressure; and that printed layer thickness decreases with retraction speed. Under these conditions, nanoparticle films with controlled thickness in the <100 nm regime can be printed using nanoporous stamp flexography, at speeds commensurate with industrial printing equipment.

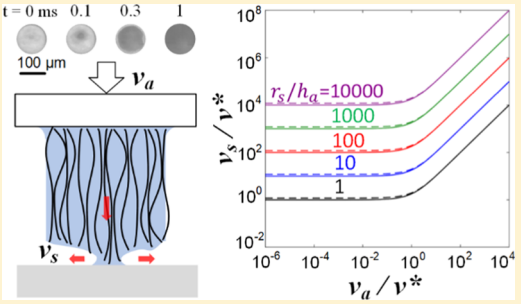

INTRODUCTION

High-throughput printing of electronic materials is critical to mass production of devices including thin film transistors,[1−5] RFID tags,[6] and transparent electrodes, for use in applications such as smart packaging,[7−10] asset tracking, and photovoltaics.[11,12] Typically, the desired formats of printed electronics contrast those of wafer-based semiconductor fabrication, demanding lower manufacturing cost and large-area compatibility.[1,6,13−15] Many traditional printing technologies, including inkjet, flexography, gravure, slot die coating, and screen printing, have been adapted to the printing of inks suited as precursors to functional thin films. The performance of devices, such as printed transistors and the resolution of printed display pixels, is in particular limited by the performance of extant printing methods. For instance, flexography (Figure 1A) is a highly scalable, high-speed direct printing method, yet it is limited to resolutions of ∼10's of microns[16] as a result of the ink being squeezed out[17,18] between the stamp and substrate and due to dewetting of the deposited ink film.[19] Broadly, there remains an important need for improved printing technologies for ultrathin (∼0.1 μm or smaller) and fine features (∼μm resolution) to advance printed electronics technology.

Most of the aforementioned printing technologies use liquid or polymeric inks, often containing colloidal nanoparticles that are sintered to form films after drying of the printed ink pattern. As such, limitations to the feature size and thickness are attributed to the coupled, time-dependent fluid and solid mechanics of the printing process. In flexographic printing, we recently demonstrated that significantly finer printed feature dimensions can be achieved when nanoporous stamps are used instead of traditional nonporous polymer stamps.[20] The key difference is that nanoporous stamps retain the ink within their volume (Figure 1B), enabling the printed pattern to precisely replicate the shape of stamp features without suffering the squeeze-out and dewetting instabilities of traditional flexography. For instance, nanoporous stamps comprising polymer-coated vertically aligned carbon nanotubes (CNTs) enabled

Received: February 15, 2019
Revised: April 17, 2019
Published: April 23, 2019

DOI: 10.1021/acs.langmuir.9b00460
Langmuir 2019, 35, 7659−7671

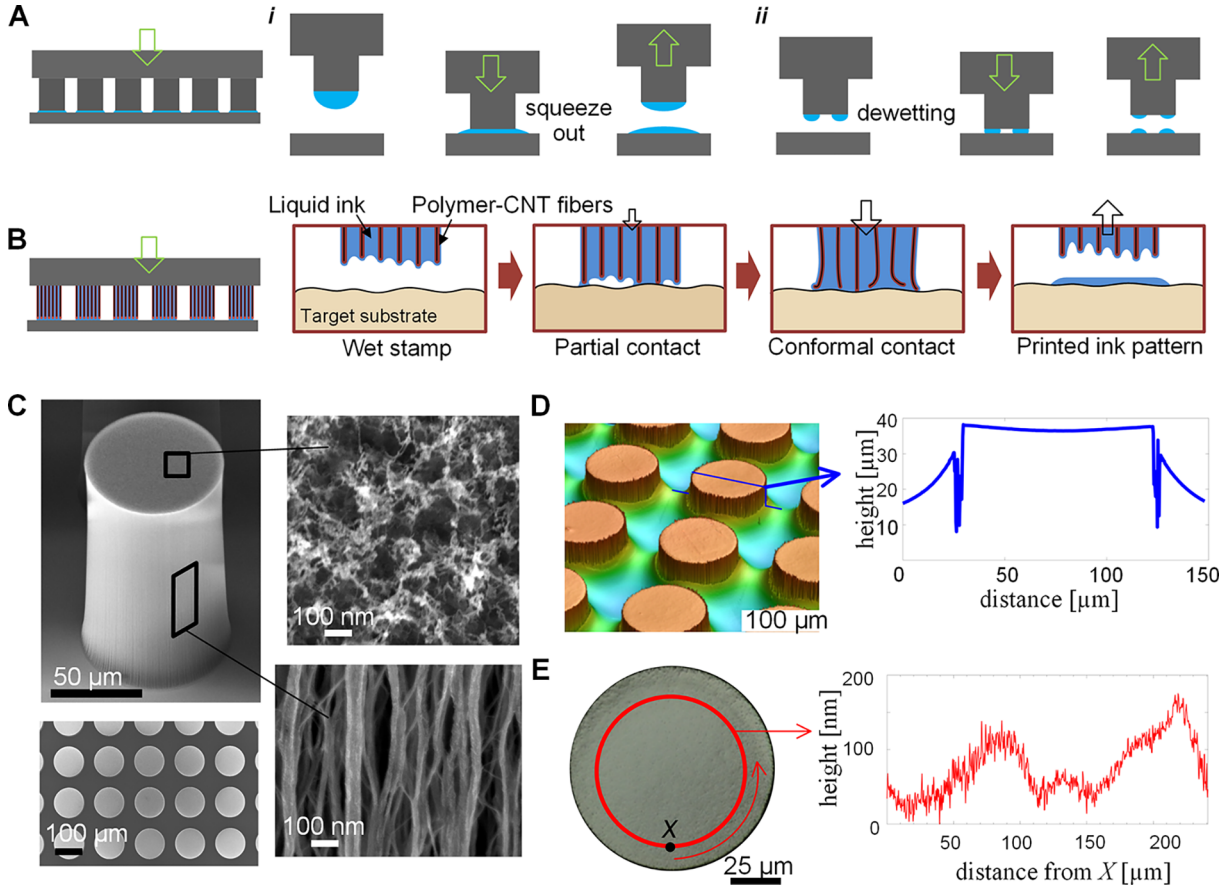

Figure 1. Nanoporous stamps for ultrathin flexographic printing. (A) Spreadout and film dewetting lead to loss of resolution and uniformity in flexography with non-porous elastomer stamps. (B) Simplified schematic of ink transfer from carbon nanotubes (CNTs) micropillar stamp loaded with ink. (C) Scanning electron microscope images of typical circular CNT micropillar array (100 μm pillar diameter, 150 μm height) used for nanoporous flexography; close-up top and side surfaces of a micropillar reveal pores with ~100 nm width. (D) Confocal microscope images of the stamp after infiltration of Ag (in tetradecane) nanoparticle ink. The 2D profile shows the wetted liquid surface around the stamp pattern. (E) Top view confocal microscope image of a single micropillar and height profile extracted from the image.

high-speed (0.1 m/s) printing of features with ~3 μm minimum size, from conductive, dielectric, and semiconducting nanoparticle inks.

In traditional flexography, when the elastomer printing stamp is brought into contact with the substrate, the ink on the surface of the stamp forms a liquid bridge between the stamp and the substrate. As the stamp and substrate are separated, the liquid bridge ruptures, and a small volume of liquid is transfered to the substrate under each stamp feature. Early studies of liquid transfer in flexography, using millimeter-scale features and glycerol showed that the relative contact angles between the liquid and the surfaces determined the transfer fraction under quasi-static conditions.[21,22] Fast separation led to the liquid separating equally between the two surfaces irrespective of the wettability.[23] Experiments using distilled water, poly(methyl methacrylate) stamps, and a variety of acceptor surfaces established that the difference in the receding contact angles of the donor and acceptor surfaces determines the transfer ratio at low separation speeds.[24−26] Amirfazli et al. also studied the combined effects of inertia, ink viscosity, and receding contact angles on the liquid transfer and developed empirical relations for the transfer ratio as a function of capillary number (Ca = 10^{-7} to 1), Reynolds number (Re = 10^{-8} to 10^{2}), and contact angles (θ = 30−113°).[27−29] Qian and Breuer[30] developed mathematical models validated by their experiments to study the liquid transfer from a constant volume liquid bridge between a donor surface where the contact line is pinned and a hydrophobic acceptor surface where the contact line is free to move. They used stability analysis to predict the onset of contact line motion and the onset of bridge rupture and thereby predicted the influence of drop volume on the transfer ratio. In summary, at low speeds, the receding contact angles on the two surfaces determine the ink transfer ratio, with a greater fraction remaining on the surface with higher wettability. As the speed increases, the process becomes less dependent on surface properties and the transfer ratio tends toward 50%. The transfer ratio decreases at even higher speeds due to the volume lost to the formation of satellite droplets during rupture. Yet, nonuniform drying and capillary flow produce printed features with nonuniform thickness, which remains a limitation to the practical use of flexography in printed electronics.

Using nanoporous stamps, we may expect that the relative wettability and separation speed will similarly be important, yet the role of the stamp texture and porosity on the formation and recession of the liquid−solid interface during printing can influence the speed limits of the process as well as the amount of ink transferred. Here, we study the dynamics of ink transfer between nanoporous stamps and solid substrates. We capture the printing process with a high-speed, high-magnification

DOI: 10.1021/acs.langmuir.9b00460
Langmuir 2019, 35, 7659−7671

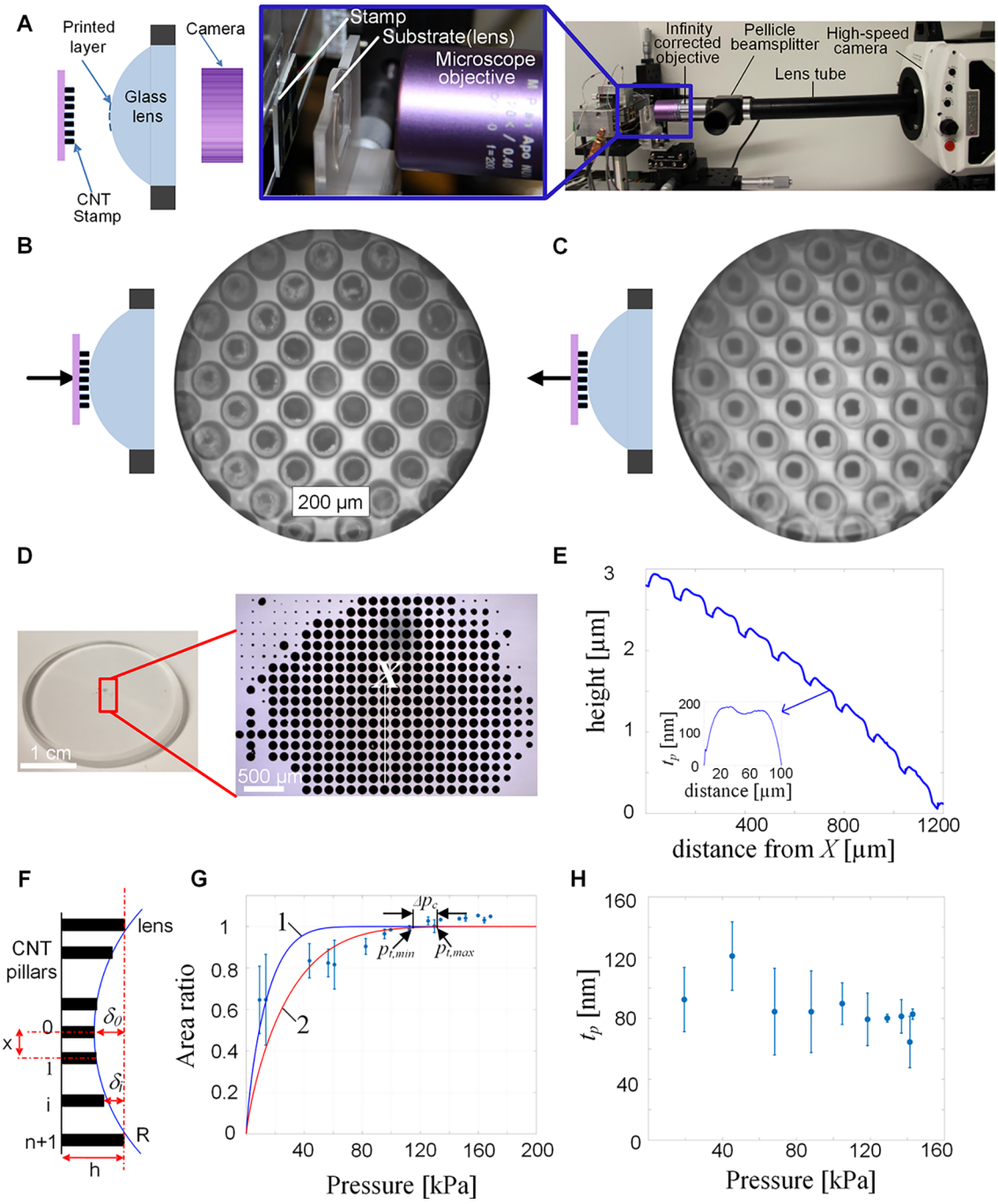

Figure 2. Experimental setup and procedures for the visualization of liquid transfer. (A) Apparatus where contact between the stamp and a spherical lens is imaged through the back side of the lens using a high-speed camera. (B, C) Snapshots from an exemplary experiment during the approach of the stamp and retraction of the stamp from the lens, respectively. The stamp pattern is an array of 100 μm circles with 30 μm spacing, and the experiment is shown in Videos S1 and S2. (D) Pattern printed onto the lens. (E) The surface profile of the printed patterns measured by a stylus profilometer after the solvent evaporation, along the line indicated in (D). (F) Schematic showing the compression of stamp pillars when in contact with the spherical lens. (G) The calculated area ratio of patterns printed on lens versus contact pressure and comparison with contact model (λ_{CNT} = 45 nm, σ_l = 30 nm, and λ_{CNT} = 45 nm, σ_l =15 nm are the parameter values in Models 1 and 2,[20] respectively). (H) The measured thickness of printed layers versus calculated contact pressure at the retraction speed of 0.3 mm/s.

imaging apparatus positioned behind a transparent substrate. Based on image analysis and analytical modeling, we then discuss the dynamics of ink spreading, recession, and respreading during printing. These findings provide guidance to control the uniformity and thickness of printed patterns and to assess the potential rate and scale limits that are critical to industrial applicability of the technology.

METHODS

Visualized Printing Experiments. The experimental setup was designed to accommodate CNT stamps up to 20 × 20 mm in size, to control the contact force, stamp approach, retraction speeds, and alignment between the stamp and the substrate. During printing, the CNT stamp is placed on the flexure stage, and the printing substrate is placed in a circular slot of an acrylic fixture. The flexure is clamped at its ends and a capacitance probe placed between the flexure holder

DOI: 10.1021/acs.langmuir.9b00460
Langmuir 2019, 35, 7659−7671

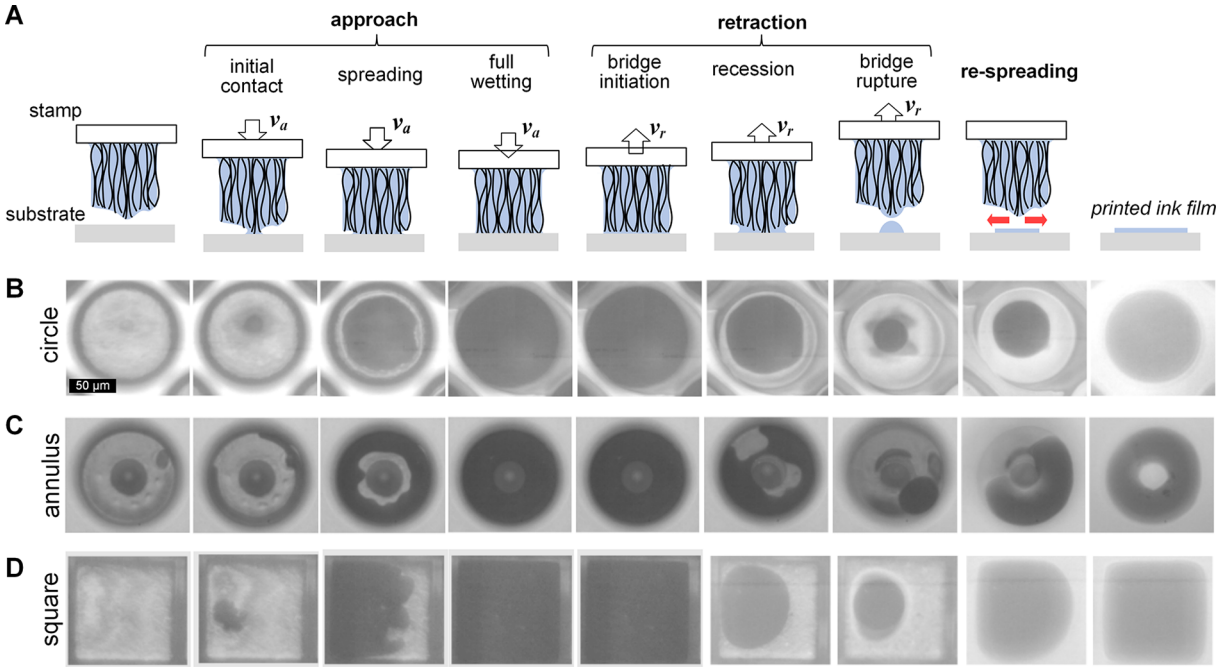

Figure 3. Visualization of ink transfer. (A) Schematic sequence of steps as observed by the high-speed imaging. Images corresponding to each step from videos of (B) 100 μm circular stamp (videos in S3a−c), (C) annular stamp with 100 μm outer diameter and 30 μm inner diameter (videos in S4a−c), and (D) square with 100 μm side length (videos in S5a,b).

and the flexure is used to measure the deflection and set the contact force between the stamp and substrate. The flexure holder is attached to a single axis motion stage via a tip-tilt stage which is used to align the stamp with the substrate. The printing substrate is a spherical lens. A custom-built microscope along with a high-speed camera (Vision Research, Phantom v2511) was placed behind the substrate and was used to take videos during the printing experiments. The dry stamp is placed on the flexure and is brought into contact with the spherical lens so that the contact pressure on the stamp is within the range[20] required to achieve conformal contact, and the stamp is aligned with the substrate. The stage displacement required to achieve the contact pressure is recorded, and the stamp is removed from the flexure. After inking and excess ink removal, as outlined in the inking section, the wet stamp is placed on the flexure and brought into contact with the lens. During such a printing step, including stamp approach and retraction, high-speed videos are recorded at up to ~25 000 frames per second.

Stamp Fabrication. To fabricate the stamps,[20] first vertically aligned CNT arrays (CNT "forests") are grown on lithographically patterned silicon substrates by atmospheric pressure chemical vapor deposition (CVD). Then, the top-entangled "crust" layer (<1 μm thickness) is removed by a brief oxygen plasma etching (Diener, Femto Plasma System) and coated with a thin layer (~20 nm) of poly-perfluorodecylacrylate (pPFDA) using initiated CVD (iCVD).[20,31,32] The plasma etching is critical to remove the stiff and rough crust which is not desirable for high-resolution printing because it results in nonuniform contact against the target substrate. The pPFDA coating followed by second plasma treatment allow liquid infiltration and solvent evaporation without shrinkage or collapse of the CNT forest by elastocapillary densification. The final plasma-treated pPFDA-CNT microstructures are highly porous (>90% porosity) with nanometer pore size (~100−200 nm), allowing liquid infiltration without deformation due to capillary forces, and are mechanically compliant, enabling uniform contact with the target substrates.

Inking. The ink used in this study is composed of silver nanoparticles dispersed in tetradecane (Sigma-Aldrich, 736511). The surface tension and viscosity of the ink are 27 mN/m and 10 mPa s, respectively, and the ink exhibits good conductivity (30−60% of bulk silver) after annealing.[20] The particle concentration is 50−60 wt % with particle sizes less than 10 nm. A 100 μL droplet of ink is pipetted onto the stamp, and then the stamp is spun to 1500 rpm for 1−3 min in a spincoater.

RESULTS AND DISCUSSION

Nanoporous stamps are fabricated by chemical vapor deposition (CVD) growth of CNT forests from a lithographically patterned catalyst film on a silicon wafer (see Methods). An exemplary stamp with an array of cylindrical micropillars is shown in Figure 1C. The mechanical compliance, surface roughness, and wettability of the stamp structures are tailored via plasma treatment of the CNTs and subsequent coating with a thin layer of polymer (pPFDA, 20 nm) by initiated chemical vapor deposition (iCVD).[20,31,32] The combined treatment allows liquid inks to wick inside the structures without significant densification or swelling (Figure 1D,E). The wet stamp has ink infiltrated in the stamp microstructures and in the gaps between the stamp features as shown in the microscope image (Figure 1D) taken using a laser scanning confocal microscope (Keyence, VK-X250). In order to remove the ink in the gaps, we bring the wet stamp into contact with another stamp consisting of CNT forests with no patterns in them, as described in our previous work.[20] The stamp after the removal of excess ink has ink wetting the stamp surface conformally, as shown in the confocal microscope image (Figure 1E).

Ink transfer from the nanoporous stamps to glass substrates is visualized using a custom-built printing apparatus integrated with a high-magnification, high-speed imaging system (Figure 2A). A colloidal silver nanoparticle ink (Sigma-Aldrich, <10 nm in tetradecane, 50−60 wt %) was used in all experiments, and the ink was applied to the stamp by pipetting a 100 μL drop on the stamp followed by spin coating at 1500 rpm for 3 min.[20] In each experiment, an inked stamp was brought into contact with a spherical glass lens (0.50 m radius, ThorLabs) with a prescribed velocity and stopped when a prescribed force

DOI: 10.1021/acs.langmuir.9b00460
Langmuir 2019, 35, 7659−7671

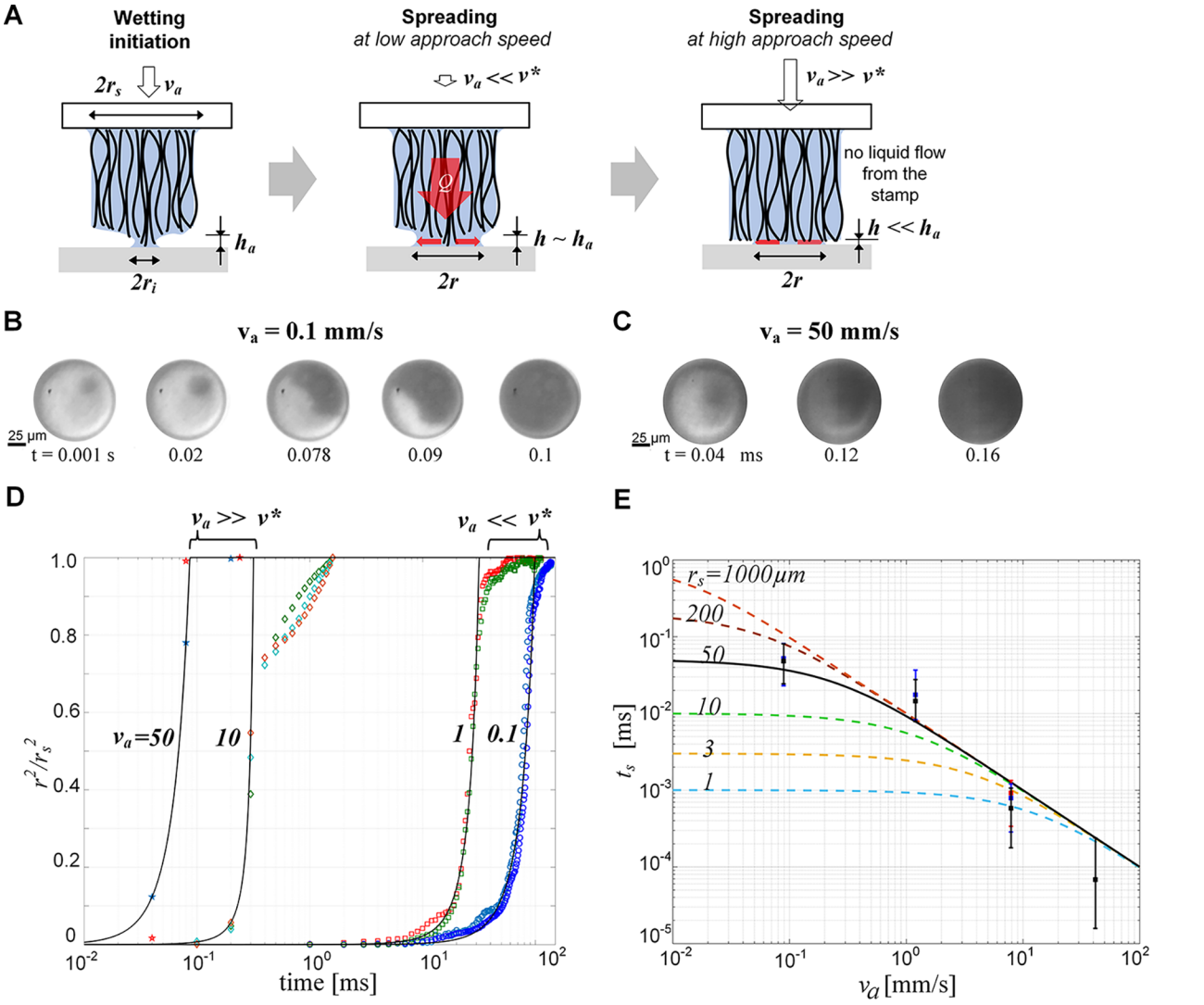

Figure 4. Spreading dynamics during the stamp approach. (A) Schematics of liquid spreading at the contact interface as the stamp approaches the substrate, wetting initiation and spreading at low ($v_a \ll v^*$) and high approach speeds ($v_a \gg v^*$). (B) Snapshots from the high-speed videos showing the liquid spreading on the substrate at different approach speeds of 0.1 mm/s (C) and 50 mm/s. (D) Ratio of the area covered by spread liquid to stamp area plotted as a function of time elapsed since wetting initiation for four different approach speeds, 0.1, 1, 10, 50 mm/s (solid lines are based on eq 2 and dots represent experimental data from videos shown in S6a–d). (E) Average spreading time of the liquid versus stamp approach speed (dashed lines show modeling predictions for different stamp radii and the solid line is that for stamp radius of 50 μm. The dots and error bars are the average and standard deviation of experimental data using a stamp radius of 50 μm).

was reached (see Methods). Contact was maintained at the specified force for 10 s, then the stamp was retracted from the lens with a second prescribed velocity. The stamp–substrate interface was viewed through the back (flat) side of the lens during the entire printing process (Figure 2B,C and Videos S1 and S2). The convex curvature of the lens ensured a contact region with locally uniform pressure, being essentially flat in comparison to the size of the individual stamp micropillars. In Figure 2D,E we show an exemplary printed pattern and thickness profile on the lens after solvent evaporation. When the micropillar array stamp contacts the lens, each micropillar prints a circular feature and is compressed by an amount determined by the position of the stamp along the motion axis and the local position of the lens surface where it contacts the micropillar (Figure 2F). As a result, a single experiment creates an array of printed features under locally different contact pressures, and correlations between contact pressure, print thickness, and print area (relative to the micropillar area) are assessed (Figure 2G,H). The print area ratio (the ratio of the area of the stamp pattern to printed pattern) increases with the contact pressure (Figure 2G), whereas the measured thickness (Figure 2H) of the printed layers is not influenced by the contact pressure. Thus, the videos must be used to understand the dynamics of ink transfer.

From the videos, we identify the dynamics of contact and ink transfer between the stamp and substrate, as shown in Figure 3 and Videos S3a–c, S4a–c, S5a,5b, for individual inked micropillars with circular, annular, and square shapes. Upon initial contact between the micropillar and substrate, wetting initiates; the position of contact is determined by the surface profile of the micropillar stamp, which has a waviness of ~1 μm over 100 μm. Then, the liquid spreads outward to fill the gap between the stamp and substrate, whereas the stamp continues to approach the surface. For the circular micropillar (Figure 3B) of radius r_s, the liquid spreads radially outward ($r(t)$). For the annular stamp (Figure 3C), initial contact

DOI: 10.1021/acs.langmuir.9b00460
Langmuir 2019, 35, 7659–7671

occurred along the outer circumference, followed by liquid spreading along a ring which expanded to fill the annulus. For the square stamp (Figure 3D), spreading began near the left edge of the image, then reached the top and bottom edges, and then swept to the right. In all cases, the rate and direction of spreading are influenced by the local gap height and stamp waviness, until spreading stops when the liquid is pinned by the edge of the stamp feature. According to the experiment procedure, the motion of the stamp is stopped when the prescribed contact pressure is reached; here, the local pressure ensured that the stamp contact area became fully wetted. Contact may remain partial if the pressure is insufficient, which results in incomplete wetting and thus nonuniform printing.[20]

When retraction of the stamp begins, a liquid bridge forms, pinned to the edges of the stamp and filling the small gap. As retraction continues, the liquid bridge recedes inward until it ruptures and leaves a droplet on the substrate. After the rupture of the liquid bridge, the separated drop respreads back to the original shape that was wetted during the stamp contact. This behavior is particularly evident when we observe the annular and square stamps and appears to be critical to the shape the fidelity of the printing process. Below, we further discuss each stage of observation and understand the governing attributes of the liquid transfer dynamics and the printed liquid volume.

Initial Contact ($r_i \ll r_s$). At the instant of first contact between a small area of the stamp and the substrate, a liquid bridge forms, as in Figure 4A. If the stamp is inked conformally (Figure 1D), such that there is not an excess layer of liquid on its top surface,[20] the point of initial contact is the "highest" point on the stamp determined by the waviness of the polymer-coated CNT forest. The stamp may have micron-scale waviness due to nonuniformity in the CNT growth and has nanoscale roughness (Figure 1E, $\sigma \sim 50$ nm) due to the height variation of the CNTs after the growth, coating, and plasma treatment. Stamp waviness and angular alignment with the substrate both produce micron-scale variations in gap height across the stamp feature and collectively determine the initial gap height (h_a) at which the liquid bridge forms.

Spreading ($r_i < r < r_s$). Spreading (Figure 4B) between the nanoporous stamp and substrate is fundamentally different from that between two solid surfaces[17,24,26−28,30] (as in classical flexography); here, one surface is porous and filled with liquid, allowing a liquid supply to the gap during spreading. Accordingly, the volume of liquid between the stamp and the substrate may continuously change during the spreading step. Considering a small volume of liquid in a gap closing at a constant speed (v_a) with height of $h = h_a - v_a t$, we equate the rate of volume change of the liquid within the gap to the flow rate from the porous medium (see Supporting Information)

$$\frac{\mathrm{d}}{\mathrm{d}t}(\pi r^2 h) = \frac{4\Delta P\sqrt{k_{zz}k_{rr}}}{\mu} r \tag{1}$$

Here, ΔP [Pa] is the pressure difference from deep in the porous stamp to the outer radius of the liquid meniscus in the gap, μ [Pa s] is the ink viscosity, and k_{zz} and k_{rr} [m^2] are the axial and radial permeabilities of the stamp. The term on the right is the approximate flow rate from a semi-infinite, anisotropic porous medium driven by a pressure difference.[33−35] We approximate the stamp near the contact interface as a porous medium consisting of parallel cylinders,[34] for which, to leading order, $k_{rr} \approx k_{zz}/2$. The pressure in the gap is lower than that in the stamp, and this difference provides the driving force for the ink flow during spreading. The pressure difference is estimated as $\sim \gamma/\lambda_{CNT}$, where γ [N/m] is the surface tension of the ink and λ_{CNT} is the CNT−CNT spacing, and is taken to be constant during spreading. Solving eq 1 (see Supporting Information), we derive the time-varying radius of the ink in the gap as

$$\frac{r}{r_s} = \frac{2v^*}{v_a}\left(1 - \frac{v_a t}{h_a}\right)^{-1/2} - \frac{2v^*}{v_a} \tag{2}$$

where v^* is a critical velocity

$$v^* = \frac{2\Delta P\sqrt{k_{rr}k_{zz}}}{\pi\mu r_s} \tag{3}$$

To validate this model, we conducted printing experiments at approach speeds ranging from 0.1 to 50 mm/s. From the high-speed video images (Figures 4B,C), an effective spreading radius is extracted and compared to the model (Figure 4D). For $r^2/r_s^2 < 0.95$, the model captures the general trends in the experimentally measured spreading profiles for both low and high approach speeds. Here, v^* and h_a are used as fitting parameters to match the model to the measured curves. Ink loading determines the precise value of ink pressure within the stamp (ΔP) and will contribute to variations in v^* (eq 3) between prints.

As r^2/r_s^2 approaches unity, spreading slows, and our model does not account for how the liquid comes to rest. One contributing factor is the approximation of symmetric spreading; while we model spreading as always starting at the center of a radially symmetric geometry, the initial liquid bridge usually initiates at least slightly off-center, as seen in Figure 4B,C. Therefore, at short times relative to the total spreading time, the radial approximation is valid; yet once the ink reaches an edge, the spreading becomes asymmetric and deviates from the model predictions. Since ink does not flow beyond the edge, the average spreading rate slows, as seen at later times in Figure 4D.

Moreover, at low approach speeds, the rate of spreading is approximately constant, while at higher approach speeds, the rate of spreading is proportional to approach speed, Figure 4E. We classify these as capillary and compression driven spreading, respectively. Defining the average velocity of the spreading meniscus $v_s = r_s/t_s$, where t_s the total spreading time, eq 1 gives

$$\frac{v_s}{v^*} = \frac{r_s}{h_a}\frac{v_a}{v^*}\left[1 - \left(1 + \frac{v_a}{2v^*}\right)^{-2}\right]^{-1} \tag{4}$$

By taking low and high-speed limits of eq 2

$$v_s = \begin{cases} \dfrac{r_s}{h_a} v^* & \text{when} \dfrac{v_a}{v^*} \ll 1 \\ \dfrac{r_s}{h_a} v_a & \text{when} \dfrac{v_a}{v^*} \gg 1 \end{cases} \tag{5}$$

Therefore, when $v_a \ll v^*$, capillary driven flow from the porous stamp dominates the spreading rate, and spreading can be approximated as if the stamp was stationary (Figure 4B). For $v_a \gg v^*$, however, the gap is closing at a much faster rate than the rate at which ink can flow from the stamp (Figure 4C). In this

DOI: 10.1021/acs.langmuir.9b00460
Langmuir 2019, 35, 7659−7671

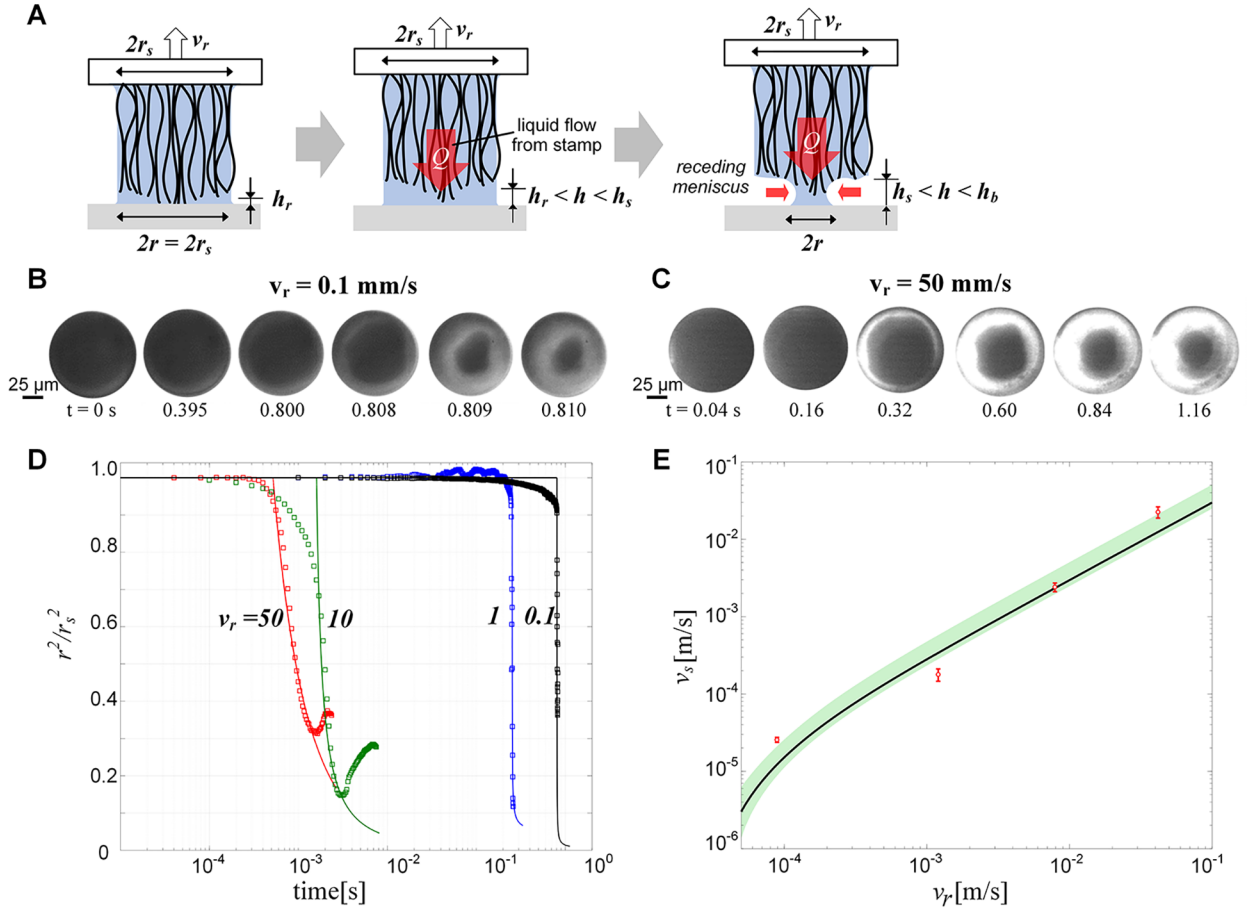

Figure 5. Receding dynamics during the stamp retraction. (A) Schematics of the liquid bridge initiation as the stamp retracts away from the substrate, contact line pinning, and recession during retraction. (B) Snapshots showing the base of the liquid bridge on the substrate at low and high retraction speeds of 0.1 mm/s (C) and 50 mm/s. (D) The ratio of the area covered by the liquid to the feature area plotted as a function of time for four different retraction speeds, 0.1, 1, 10, 50 mm/s (solid lines are based on eq 6, full videos shown in S7a–d). (E) The average recession speed of the liquid bridge versus stamp retraction speed (the bounds of the shaded region show model predictions of r_s/h_a = 10, v^*= 0.012 mm/s, and r_s/h_a = 2, v^* = 0.02 mm/s. The dots and error bars are the velocity calculated from the video observation).

regime, an initial liquid bridge that wets across the gap will undergo approximately constant volume deformation with negligible ink flow from the stamp during spreading. Therefore, the spreading rate is simply determined by the ratio of feature width to the initial gap distance and is proportional to the approach speed. Importantly, at high speeds, the spreading rate is independent of liquid properties and stamp porosity.

We estimated v^* = 0.3 mm/s using the known ink properties and approximating the stamp permeability using an analytical expression for an array of aligned cylinders[34] (see the Supporting Information). This is in reasonable agreement with the value of v^* = 0.2 mm/s used to fit the model to the measured data in Figure 4E. Differences arise due to the precise value of ink pressure within the stamp, the distribution of CNT diameters and imperfect alignment, the modeling assumption of symmetric ink spreading, and experimental uncertainty.

Full Wetting and Contact Dwell Time ($r \approx r_s$). After the stamp comes to rest, the equilibrium shape of the wetted area is determined by the contact pressure on the micropillar and by the uniformity of the stamp relative to the opposite surface. Figure 2G shows the pressure range (Δp_c) where the area ratio (ratio of the area of the stamp pattern to printed pattern) is ~1 using the measurements of printed patterns on the spherical lens and comparison with the predictive model.[20] Below the minimum threshold contact pressure ($p_{t,min}$) at the lower limit of the pressure range (Δp_c), at the end of the approach step, the contact area is less than the stamp cross-sectional area, and there are regions in the stamp–substrate interface where the gap is $\gg\lambda_{CNT}$. Therefore, there is no driving force for the flow of liquid from the stamp even with long dwell times, and the wetted area is smaller than the stamp cross-sectional area producing incomplete pattern transfer. Above the maximum threshold contact pressure ($p_{t,max}$) at the upper limit of the pressure range, excess stamp compression will squeeze out additional ink into the space between stamp features, forcing wetting over a larger area than defined by the stamp feature and resulting in oversized printed features. Therefore, when the contact pressure on the micropillar lies within the range (Δp_c), the nanoporous stamp fully contacts the opposite surface, i.e., coated CNTs are in contact throughout the area of the stamp feature.

After contact, the stamp is held against the substrate at constant force before being pulled away. During this period, the ink meniscus can relax to an equilibrium shape (ΔP = 0) through visco-capillary flow into or out of the stamp features. The relaxation likely occurs much faster than the 10 s contact time used in the experiments reported here but has not been

DOI: 10.1021/acs.langmuir.9b00460
Langmuir 2019, 35, 7659–7671

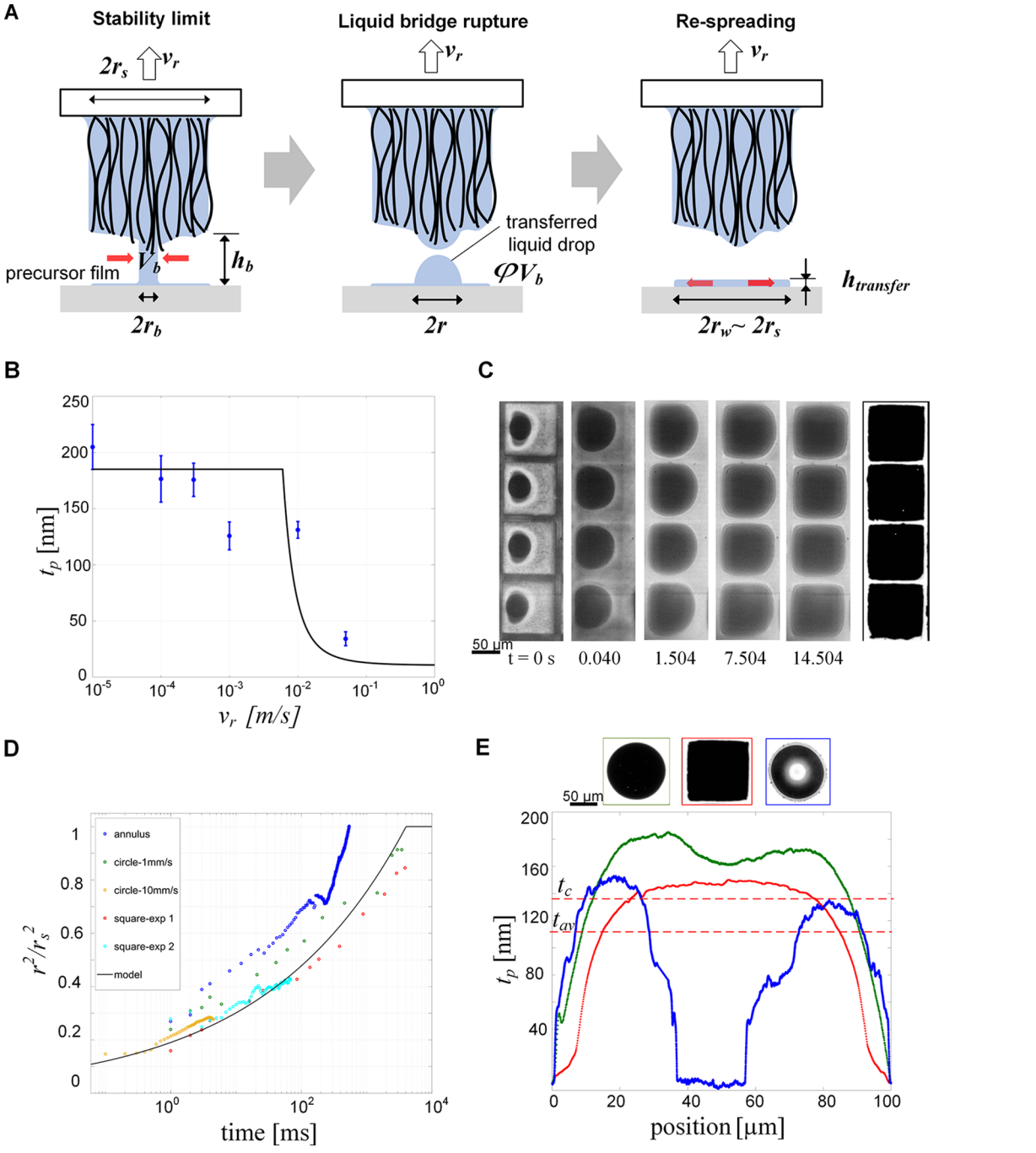

Figure 6. Transferred liquid film after bridge rupture and respreading. (A) Schematic of the liquid bridge at the moment of rupture, transferred liquid drop on the substrate after bridge rupture, and of transferred liquid drop respreading on the substrate to the stamp feature shape. (B) The thickness of printed solid layer after solvent evaporation versus retraction speed and comparison with the model (solid line) given by the eqs S-41 and S-45. (C) Snapshots from high-speed videos of respreading of transferred drops forming films with the shape of four squares matching the stamp pattern closely. (D) Ratio of respread film area to stamp area versus time for three shapes and comparison with the model in eq 7 (solid line). (E) Measured profile of printed solid layer for three shapes along with microscope images of the printed patterns.

characterized. A long contact time was used to decouple the approach and retraction stages of the printing process, but a much shorter dwell time may be used in practice and is unlikely to affect the printing results if full contact is achieved.

Retraction ($r_r < r \leq r_s$). Starting from the condition of full contact and wetting of the interface, a thin liquid bridge is initially drawn from the stamp upon retraction and is pinned to the substrate at the edges of the stamp feature (Figure 5A). At this instant, the wetted contact area remains constant, while the contact angle of the ink with the substrate decreases to the receding angle. The height of the liquid bridge within the gap when the contact line first begins to move (h_r) defines the initial volume of ink in the gap during recession. Then, the retraction speed, v_r, influences the balance between liquid bridge deformation and the flow from the porous stamp. At low retraction speeds, liquid flow from the stamp will be sufficient to maintain a filled gap between the stamp feature and the substrate as the stamp moves upward. The ink volume

DOI: 10.1021/acs.langmuir.9b00460
Langmuir 2019, 35, 7659−7671

in the gap maintains a constant radius of $r = r_s$ until the aspect ratio of the liquid bridge exceeds the stability limit, and the bridge ruptures. Equating the volume flow rate from the stamp on the right side of eq 1 to the rate of volume increase in the gap, this low-speed regime is predicted for $v_r < 2v^*$. However, during retraction, v^* may differ from that during the approach, because it is proportional to ΔP (eq 3) which has decreased during the contact dwell time.

For $v_r > 2v^*$, the meniscus will recede despite capillary pressure driven flow from the porous stamp. The radius of the receding contact can be approximated by the same method as for spreading, except here the gap height, $h = h_r + v_r t$, is increasing at a constant speed. Designating the gap height at which the ink radius begins to recede as h_r, eq 1 predicts that the ink radius decreases as

$$\frac{r}{r_s} = \frac{2v^*}{v_r} - \left(\frac{2v^*}{v_r} - 1\right)\left(1 + \frac{v_r t}{h_r}\right)^{-1/2} \quad \text{when} \frac{v_r}{2v^*} > 1 \tag{6}$$

From the high-speed video images (Figure 5B,C), an effective contact line radius is extracted and compared to the model (Figure 5D). Using v^* and h_r as fitting parameters in eq 6, model retraction curves are matched to measured time traces. In Figure 5E, we show the measured average recession speed of the contact line for different stamp retraction speeds, compared with the above model. The model curves follow the general retraction behavior but deviate from the experimental results in a few important ways. Once the contact line begins to recede, the measurements show an initially slow but accelerating motion not captured by the model (Figure 5D), whereas the model assumes that a symmetric, radial ink recession, images of the ink contact during retraction reveal a more irregular shape contributing to modeling inaccuracy. Further, the model does not account for the dynamics of the transition of a pinned contact line into a receding one. The images in Figure 5B,C suggest the possibility that the contact line initially remains pinned over some sections of the edge while receding from others, accentuating the asymmetry and resulting in a slower increase of the contact line speed as the gap increases. In the experiments, the contact line location is determined by viewing the ink through the transparent substrate. A certain thickness of ink will be required to obtain sufficient contrast to discern the contact line position. This leads to measurement uncertainty in the retraction time traces and is the greatest at the highest speed of 50 mm/s in the present experiments.

Rupture ($r = r_b$). The geometry of the receding liquid bridge and the dynamics of bridge rupture determine the liquid volume that is printed. The receding liquid bridge ruptures (Figure 6A) when the aspect ratio of the stretched meniscus exceeds its stability limit. For low capillary numbers ($Ca = \mu v_r/\gamma$), a liquid bridge with pinned contact lines stretched quasi-statically will become unstable at an aspect ratio of $h_b/r_b = 2\pi$ (r_b and h_b are the bridge radius and height at the instant of rupture, respectively) and breaks by visco-capillary necking.[36] The lowest point in Figure 5D corresponds to the instant at which the capillary bridge breaks. By analyzing the videos, we find that the radius and height at the moment of rupture reasonably agree with the quasi-static stability limit. Assuming this limit defines the moment of rupture for all retraction speeds (Ca = 0.00027−0.14), the radius, height, and volume ($V_b \sim \pi r_b^2 h_b$) of the liquid bridge at the moment of rupture can be estimated by approximating the liquid bridge geometry to be a cylinder (see Supporting Information).

The retraction profiles in Figure 5D show noticeable discrepancies in the radius of rupture between the model and the measurements. The model approximates the liquid bridge as a cylinder, but the actual liquid bridge deviates from this shape, both due to the non-circular cross-section observed in Figure 5C and the off-perpendicular contact angle it makes with the substrate. Images of the liquid bridge just after rupture (Figure 3B−D) show an off-center breaking position, indicating significant asymmetry in ink recession.

Nevertheless, we accurately predict that the volume of ink in the capillary bridge at rupture decreases with retraction speed because at higher speeds, there is less time for the ink to flow into the gap before rupture. At high speeds ($v_r \gg v^*$), ink transfer from within the stamp is negligible, and the volume at rupture plateaus to the ink volume in the gap just before the contact line recession began. The model predicts that the printed volume levels off to within 10% of the high-speed limit at v_r = 0.2 m/s and is within 2% at v_r = 1 m/s. At the limit of low speeds ($v_r \leq 2v^*$), we expect that the gap remains filled until rupture occurs. Therefore, the upper-bound for the ink transfer volume is determined by the stability limit of a liquid bridge pinned along the periphery of the stamp feature, $V_b = 2\pi^2 r_s^3$.

Moreover, the symmetry of breakage is known to strongly depend on the differences in contact angles.[28] The transferred liquid volume can simply be estimated as φV_b, where φ is the transfer ratio. Assuming subsequent drying of the ink to a uniform layer of nanoparticles, for a 50% by weight colloidal ink, we estimate the printed layer thickness (Figure 6B) as $t_p = \varphi V_b \rho_{Ag}/A\rho_{sol}$, where ρ_{Ag}, ρ_{sol} are the densities of silver and solvent and A is the area of the printed layer ($=\pi r_s^2$) (see Supporting Information). Therefore, the predicted printed layer thickness is constant for $v_r \leq 2v^*$, and then it decreases with retraction speed to level off to a constant value at high speeds ($v_r \gg v^*$). We measured the profiles (Figure 2E) of 5−10 samples of printed patterns on the spherical lens along a line and calculated the average thickness of each printed pattern. The measured values of average thickness (Figure 6B) of the printed layers are higher than 200 nm at low retraction speeds (v_r < 1 mm/s), then decrease to less than 50 nm at v_r = 50 mm/s. The initial ink volume on the stamp varies between experiments conducted at different speeds, and this leads to differences between the measured and predicted values of printed layer thickness.

Respreading ($r_b < r < r_s$). Importantly, the liquid respreads to match the stamp feature after rupture (Videos S4a−c, S5a, 5b), and therefore the nanoporous stamps can be used to produce features with internal holes (e.g., annuli) and sharp corners (Figures 6A,C) with high fidelity. We attribute this respreading to the presence of a precursor film,[37] a thin layer of liquid that forms on the wetted areas of the substrate during contact and remains after the stamp retracts. We expect this precursor film to be present even when printing with solid stamps, however, in that case, excess ink is squeezed out of the gap between the stamp and the substrate during printing, wetting a larger area than the original stamp feature. In contrast, nanoporous stamps make conformal contact with the substrate without significant squeeze out, creating a precursor film that matches the stamp area with high accuracy.

The experimental time traces of respreading (Figure 6D) show a relaxation of the ink radius without oscillation, verifying

DOI: 10.1021/acs.langmuir.9b00460
Langmuir 2019, 35, 7659−7671

that inertial effects are negligible. Droplet spreading of this type is governed by Tanner's Law[37,38]

$$\frac{r}{r_s} \propto \left(\frac{\gamma}{\mu r_s} t\right)^{1/10} \tag{7}$$

This scaling reasonably tracks the measured respreading time traces, as shown in Figure 6D. Similar to the approach and retraction models, respreading is approximated as occurring symmetrically. However, as seen in Figure 6C, the ink bridge can rupture in an off-center position with an asymmetric shape. Furthermore, the ink reaches some sections of the edge earlier than other sections. This leads to a deviation from the model throughout much of the respreading process. The model assumes radial respreading with a circular contact shape and therefore also does not resolve the slower respreading into the corners of the square feature at later times (Figure 6D). Similarly, the model does not attempt to capture the significant circumferential component of respreading from the annular feature, leading to significant deviation in that case (Figure 6D). As with the approach and retraction models, the ink is approximated as a simple fluid, but the presence of nanoparticles may further complicate the spreading dynamics especially for layers with thickness comparable to the particle size within the fluid.

Toward Precision, High-Speed Printing Using Nanoporous Stamps. Precise control of the printed layer thickness, thickness uniformity, and shape accuracy compared to the stamp features is necessary for the fabrication of devices whose performance is coupled to these parameters. Here, using nanoporous flexography, we print Ag nanoparticle films with average thicknesses ranging from <30 nm to >150 nm, at retraction speeds of 0.1−50 mm/s. Therefore, we conclude that keeping all other variables constant including the ink concentration and the surface properties, the retraction speed of the stamp is the principle means of controlling layer thickness.

Previously, we demonstrated printing at linear speeds of up to 0.2 m/s using a plate-to-roll apparatus, and this speed was limited by the operating range of the linear motion stage in our apparatus.[20,39] In the roll-to-plate configuration, which mimics industrial equipment, the retraction speed (v_r) between the stamp and the roller is

$$v_r = v_t\sqrt{(h_b/R) - (h_b/2R)^2} \tag{8}$$

where v_t and R are the tangential speed and the radius of the roller, respectively. Using values for R = 0.254 mm and v_t = 10 m/s typical in industrial flexography, we estimate the retraction speed to be 0.2 m/s which is in the asymptotic regime (t < 50 nm, Figure 6B) using the conditions of our present experiments. From this point, the printed layer thickness (after drying) may be controlled by the particle concentration in the ink.

The average thickness values calculated from the measured profiles (Figure 6E) of the printed layers of circle, square, and annulus are 146.6, 112.8, and 101.9 nm, respectively. Though the thickness tapers sharply toward the edges of each printed shape, the printed features are locally very smooth and uniform within the edge regions. The calculated (see Supporting Information) average roughness (R_a) ranges from 1.5 to 5 nm, and the RMS roughness (R_q) ranges from 2 to 7 nm. These values are at least ∼10-fold less compared to layers printed using[18,40] the conventional flexographic printing with solid elastomer stamps.

Returning to the overall distribution of printed features on the lens (Figure 2E), we find that the measured thickness of the printed layers is not influenced by the contact pressure (Figure 2H). This suggests that ink released from the stamp due to the compression of the CNTs during contact is not affecting the printed volume. It is possible that any additional ink volume released during compression is quickly reabsorbed during the decompression. This is also very desirable for industrial printing, because local and global variations in the stamp and substrate surface can be accommodated by the compliance of the stamp, without detriment to printing uniformity.

The lateral error, defined as the difference between the lateral dimension of the printed layer and that of the stamp pattern, is another major consideration for precision printing. The lateral dimension of the transferred film is determined at the moment of full wetting, as we found that the ruptured ink droplet tends to respread to fill the previously wetted shape. To achieve conformal contact between the stamp and substrate, the contact pressure between the stamp and substrate must lie within a range determined by the stiffness of the CNTs, CNT−CNT spacing (λ_{CNT}), and the standard deviation (σ_l) of the lengths of CNTs, assuming that the lengths are normally distributed.[20] Figure 2G shows the pressure range (Δp_c) where the area ratio (ratio of the area of stamp pattern to printed pattern) is ∼1 using the measurements of printed patterns on the spherical lens and comparison with the predictive model.[20] At the moment of full wetting, if the contact pressure is within this range, then during respreading, the transferred liquid drop fills the wetted area that matches the stamp pattern. If the pressure is less than the lower limit of this range, the printed area will be less than the stamp area due to partial or incomplete contact between the stamp and substrate. When the pressure is greater than the upper limit of this range, the area ratio is greater than 1 due to excessive deformation of the nanoporous stamp. Moreover, the vertical motion precision required to maintain the contact pressure range that was experimentally determined to achieve full contact without overprinting is $2\lambda_{CNT}^2\Delta p_c/k_{cnt}$, where k_{cnt} is the stiffness of the CNT. Therefore, the motion precision required is ∼150 nm to minimize lateral error in printing.

Limitations of This Study. Our liquid transfer model elucidates other key factors that determine the transfer behavior and resulting dimensions of the transferred film, such as liquid surface tension and viscosity, stamp permeability, and initial ink load on the stamps. Further insights can be gained by studying the effect of the stamp porosity by varying the coating thickness of polymer on the CNTs or the CNT diameter or by varying both. However, varying the porosity by these methods will change the stiffness of the stamp and hence will alter the stamp−substrate contact mechanics. Experimental validation using inks with a wide range of liquid properties and stamps with controlled pore sizes will be beneficial for further understanding.

Also, colloidal nanoparticle inks exhibit shear thinning rheology dependent on particle concentration.[41−51] This non-Newtonian behavior remains small for particle volume fractions below 25%,[44] making a Newtonian flow approximation reasonable for the 7% volume fraction ink used in this study. However, printing with inks at higher loading and/or printing of much smaller features may require consideration of

DOI: 10.1021/acs.langmuir.9b00460
Langmuir 2019, 35, 7659−7671

non-Newtonian behavior. The assumption of Newtonian flow is further justified in section 6 of the Supporting Information.

The influence of stamp compression on the ink flow within the gap, and the dynamics of retraction must be considered for features whose dimensions approach the motion and alignment precision of the printing apparatus or when stamp compression is relied upon to accommodate substrate curvature or roughness. Further, the present model approximates the ink volume in the gap as being cylindrical and groups a number of factors including capillary pressure within the stamp, contact angles, and ink loading into a fitting parameter, ΔP, without attempting to find a relation for this parameter based on the physical system. Nevertheless, our analysis captures the key dependencies of transferred ink volume on retraction speed and of spreading time on approach speed.

CONCLUSIONS

We have studied the dynamics of ink transfer from nanoporous stamps enabling precision printing of ultra-thin liquid films by displacement-controlled mechanical contact. Using high-speed imaging and analytical modeling, we have shown that at low stamp approach speeds, liquid spreading is driven by capillary forces and flow from the nanoporous stamp, while at high approach speeds, liquid spreading is driven by the stamp compression rate during contact. The same model was applied to retraction to show how the flow within the stamp influences the volume of liquid transferred at different stamp speeds. Further, we show how the respreading of liquid over a precursor film, matching the maximal stamp−substrate contact area, enables direct printing of non-circular features. These findings have implications for applying nanoporous printing stamps in industrial scale roll-to-roll printing of electronics devices. Yet, further work is required on registration and materials compatibility in multilayer printing, surface treatment to optimize wettabilities, and sintering of printed nanoparticles to form continuous layers with desired electrical properties.

ASSOCIATED CONTENT

Supporting Information

The Supporting Information is available free of charge on the ACS Publications website at DOI: 10.1021/acs.langmuir.9b00460.

Experimental setup; calculation of radius and height at the moment of rupture; list of symbols; Model of ink spreading during approach of stamp; the transfer ratio; rheological properties of colloidal nanoparticle inks; roughness of printed layer (PDF)

S1-approach-10mmpersec-1fps: (capture rate: 10 kfps, playing rate: 1 fps) the liquid spreading on the substrate when the stamp approaches it at the speed of 10 mm/s. The stamp consists of circles of 100 microns diameter and separated by 30 microns (AVI)

S2-retract-10mmpersec-10fps: (capture rate: 10 kfps, playing rate: 1 fps) the evolution of the liquid bridge when the stamp retracts from the substrate at the retraction speed of 10 mm/s. The stamp consists of circles of 100 microns diameter and separated by 30 microns (AVI)

S3a-circle-approach-1fps: (capture rate: 10 kfps, playing rate: 1 fps) (AVI)

S3b-circle-retract-before-rupture-10fps (capture rate: 10 kfps, playing rate: 10 fps) (AVI)

S3c-circle-retract-after-rupture-10fps (capture rate: 10 kfps, playing rate: 10 fps): These three videos show the (steps 1−8 outlined in Figure 3) liquid spreading during contact, liquid bridge evolution and rupture during retraction, and drop respreading on the substrate when the printing experiment is conducted with a circular stamp (AVI)

S4a-annulus-approach-100fps (capture rate: 1 kfps, playing rate: 100 fps) (AVI)

S4b-annulus-retract-before rupture-10fps (capture rate: 1 kfps, playing rate: 10 fps) (AVI)

S4c-annulus-retract-after rupture-1000fps (capture rate: 1 kfps, playing rate: 1 kfps) (AVI)

These three videos show the (steps 1−8 outlined in Figure 3) liquid spreading during contact, liquid bridge evolution and rupture during retraction, and drop respreading on the substrate when the printing experiment is conducted with a stamp of annular cross section.

S5a-approach-Squares-10fps (capture rate: 1 kfps, playing rate: 10 fps) (AVI)

S5b1-retract-Squares-1000fps (capture rate: 1 kfps, playing rate: 1k fps) (AVI)

S5b2-retract-Squares-1000fps (capture rate: 1 kfps, playing rate: 1k fps) (AVI)

These three videos show the (steps 1-8 outlined in Figure 3) liquid spreading during contact, liquid bridge evolution and rupture during retraction, and drop respreading on the substrate when the printing experiment is conducted with a stamp of square cross section.

S6a-point1mmpersec-approach-100fps (capture rate: 1 kfps, playing rate: 100 fps): The video shows the liquid spreading on the substrate when the stamp approach speed is 0.1 mm/s (AVI)

S6b-1mmpersec-approach-100fps (capture rate: 1 kfps, playing rate: 100 fps): the liquid spreading on the substrate when the stamp approach speed is 1 mm/s (AVI)

S6c-10mmpersec-approach-1fps (capture rate: 10 kfps, playing rate: 1 fps): the liquid spreading on the substrate when the stamp approach speed is 10 mm/s (AVI)

S6d-50mmpersec-approach-10fps (capture rate: 25 kfps, playing rate: 10 fps): the liquid spreading on the substrate when the stamp approach speed is 50 mm/s (AVI)

S7a-point1mmpersec-retract-100fps (capture rate: 1 kfps, playing rate: 100 fps): the base of the liquid bridge on the substrate when the stamp retracts at a speed of 0.1 mm/s (AVI)

S7b-1mmpersec-retract-10fps(capture rate: 1 kfps, playing rate: 10 fps): the base of the liquid bridge on the substrate when the stamp retracts at a speed of 1 mm/s (AVI)

S7c1-10mmpersec-retract-before-rupture-10fps (capture rate: 10 kfps, playing rate: 10 fps): the base of the liquid bridge on the substrate before rupture when the stamp retracts at a speed of 10 mm/s (AVI)

S7c2-10mmpersec-retract-after-rupture-10fps (capture rate: 10 kfps, playing rate: 10 fps): the base of the liquid bridge on the substrate after rupture when the stamp retracts at a speed of 10 mm/s (AVI)

S7d-50mmpersec-retract-100fps (capture rate: 25 kfps, playing rate: 100 fps): the base of the liquid bridge on

DOI: 10.1021/acs.langmuir.9b00460
Langmuir 2019, 35, 7659−7671

the substrate when the stamp retracts at a speed of 50 mm/s (AVI)

AUTHOR INFORMATION

Corresponding Author

*E-mail: ajhart@mit.edu.

ORCID

Dhanushkodi D. Mariappan: 0000-0002-4376-2238

Karen Gleason: 0000-0001-6127-1056

A. John Hart: 0000-0002-7372-3512

Notes

The authors declare no competing financial interest.

ACKNOWLEDGMENTS

Financial support was provided by the National Science Foundation (CMMI-1463344, CMMI-1826216), the MIT Energy Initiative Seed Fund, the MIT-Skoltech Next Generation Program, and BAE Systems. We thank Prof. L. Mahadevan of Harvard University for discussion regarding the ink transfer model; Dr. Jim Bales, Mark Belanger, and the MIT Edgerton Center for providing the high-speed camera and for the fabrication support; Steve Wasserman for assistance designing the optics for the high-speed imaging system; Brij Bhushan for assistance with image processing; and Henri Louis Girard for discussions on liquid spreading. CNT catalyst deposition and patterning were performed at the MIT Microsystems Technology Laboratory (MTL). Electron microscopy and profilometry were performed at the shared experimental facilities at the MIT Center for Materials Science and Engineering (CMSE) supported in part by the MRSEC Program of the National Science Foundation under award number DMR-1419807. Confocal microscopy was performed at the Institute for Soldier Nanotechnologies at MIT supported in part by the US Army Research Office under Cooperative Agreement Number W911NF-18-2-0048.

REFERENCES

(1) Homenick, C. M.; James, R.; Lopinski, G. P.; Dunford, J.; Sun, J.; Park, H.; Jung, Y.; Cho, G.; Malenfant, P. R. L. Fully Printed and Encapsulated SWCNT-Based Thin Film Transistors via a Combination of R2R Gravure and Inkjet Printing. *ACS Appl. Mater. Interfaces* **2016**, *8*, 27900−27910.

(2) Grubb, P. M.; Subbaraman, H.; Park, S.; Akinwande, D.; Chen, R. T. Inkjet Printing of High Performance Transistors with Micron Order Chemically Set Gaps. *Sci. Rep.* **2017**, *7*, No. 624.

(3) Park, J.; Kim, M.; Yeom, S.-W.; Ha, H. J.; Song, H.; Min Jhon, Y.; Kim, Y.-H.; Ju, B.-K. Flexible Ambipolar Organic Field-Effect Transistors with Reverse-Offset-Printed Silver Electrodes for a Complementary Inverter. *Nanotechnology* **2016**, *27*, No. 225302.

(4) Byun, K.; Subbaraman, H.; Lin, X.; Xu, X.; Chen, R. T. A 3 μm Channel, Ink-Jet Printed CNT-TFT for Phased Array Antenna Applications. In Proceedings of the 2013 IEEE Texas Symposium on Wireless and Microwave Circuits and Systems, WMCS, 2013.

(5) Zhou, Y.; Gaur, A.; Hur, S.-H.; Kocabas, C.; Meitl, M. A.; Shim, M.; Rogers, J. P-Channel, N-Channel Thin Film Transistors and P−n Diodes Based on Single Wall Carbon Nanotube Networks. *Nano Lett.* **2004**, *4*, 2031−2035.

(6) Want, R. RFID A Key to Automating Everything. *Sci. Am.* **2004**, *290*, 56−65.

(7) Kim, Y.; Chortos, A.; Xu, W.; Liu, Y.; Oh, J. Y.; Son, D.; Kang, J.; Foudeh, A. M.; Zhu, C.; Lee, Y.; et al. A Bioinspired Flexible Organic Artificial Afferent Nerve. *Science* **2018**, *360*, 998−1003.

(8) Kuzum, D.; Takano, H.; Shim, E.; Reed, J. C.; Juul, H.; Richardson, A. G.; De Vries, J.; Bink, H.; Dichter, M. A.; Lucas, T. H.; et al. Transparent and Flexible Low Noise Graphene Electrodes for Simultaneous Electrophysiology and Neuroimaging. *Nat. Commun.* **2014**, *5*, No. 1628.

(9) MacKin, C.; Palacios, T. Large-Scale Sensor Systems Based on Graphene Electrolyte-Gated Field-Effect Transistors. *Analyst* **2016**, *141*, 2704−2711.

(10) Debéda, H.; Lucat, C.; Pommier-Budinger, V. Printed Piezoelectric Materials for Vibration-Based Damage Detection. *Procedia Eng.* **2016**, *168*, 708−712.

(11) Søndergaard, R.; Hösel, M.; Angmo, D.; Larsen-Olsen, T. T.; Krebs, F. C. Roll-to-Roll Fabrication of Polymer Solar Cells. *Mater. Today* **2012**, *15*, 36−49.

(12) Krebs, F. C. Fabrication and Processing of Polymer Solar Cells: A Review of Printing and Coating Techniques. *Sol. Energy Mater. Sol. Cells* **2009**, *93*, 394−412.

(13) Allen, B. L.; Kichambare, P. D.; Star, A. Carbon Nanotube Field-Effect-Transistor-Based Biosensors. *Adv. Mater.* **2007**, *19*, 1439−1451.

(14) Song, D.; Zare Bidoky, F.; Hyun, W. J.; Walker, S. B.; Lewis, J. A.; Frisbie, C. D. All-Printed, Self-Aligned Carbon Nanotube Thin-Film Transistors on Imprinted Plastic Substrates. *ACS Appl. Mater. Interfaces* **2018**, *10*, 15926−15932.

(15) Cosnahan, T.; Watt, A. A. R.; Assender, H. E. Modelling of a Vacuum Metallization Patterning Method for Organic Electronics. *Surf. Coatings Technol.* **2018**, *336*, 128−132.

(16) Moonen, P. F.; Yakimets, I.; Huskens, J. Fabrication of Transistors on Flexible Substrates: From Mass-Printing to High-Resolution Alternative Lithography Strategies. *Adv. Mater.* **2012**, *24*, 5526−5541.

(17) Darhuber, A. A.; Troian, S. M.; Wagner, S. Physical Mechanisms Governing Pattern Fidelity in Microscale Offset Printing. *J. Appl. Phys.* **2001**, *90*, 3602−3609.

(18) Kattumenu, R. C. Flexography Printing of Silver Based Conductive Inks on Packaging Substrates; West Michigan University, PhD Thesis, 2008.

(19) Johnson, J. Aspects of Flexographic Print Quality and Relationship to Some Printing Parameters; Karlstads Universitet, PhD Thesis, 2008.

(20) Kim, S.; Sojoudi, H.; Zhao, H.; Mariappan, D.; McKinley, G. H.; Gleason, K. K.; Hart, A. J. Ultrathin High-Resolution Flexographic Printing Using Nanoporous Stamps. *Sci. Adv.* **2016**, *2*, No. e1601660.

(21) Chadov, A. V.; et al. Investigation of the Transfer of a Liquid from One Solid Surface to Another. I. Slow Transfer. Method of Approximate Calculation. *Kolloidn. Zh.* **1979**, *41*, 700−703.

(22) Kumar, S. Liquid Transfer in Printing Processes: Liquid Bridges with Moving Contact Lines. *Annu. Rev. Fluid Mech.* **2015**, *47*, 67−94.

(23) Yakhnin ED, C. A. Investigation of the Transfer of a Liquid from One Solid Surface to Another. II. Dynamic Transfer. *Kolloidn. Zh.* **1983**, *41*, 1034−39.

(24) Chen, H.; Tang, T.; Amirfazli, A. Liquid Transfer Mechanism between Two Surfaces and the Role of Contact Angles. *Soft Matter* **2014**, *10*, 2503−2507.

(25) Chen, H.; Amirfazli, A.; Tang, T. Modeling Liquid Bridge between Surfaces with Contact Angle Hysteresis. *Langmuir* **2013**, *29*, 3310−3319.

(26) Chen, H.; Tang, T.; Zhao, H.; Law, K.-Y.; Amirfazli, A. How Pinning and Contact Angle Hysteresis Govern Quasi-Static Liquid Drop Transfer. *Soft Matter* **2016**, *12*, 1998−2008.

(27) Chen, H.; Tang, T.; Amirfazli, A. Fast Liquid Transfer between Surfaces: Breakup of Stretched Liquid Bridges. *Langmuir* **2015**, *31*, 11470−11476.

(28) Chen, H.; Tang, T.; Amirfazli, A. Effects of Surface Wettability on Fast Liquid Transfer. *Phys. Fluids* **2015**, *27*, No. 112102.

(29) Huang, C. H.; Carvalho, M. S.; Kumar, S. Stretching Liquid Bridges with Moving Contact Lines: Comparison of Liquid-Transfer Predictions and Experiments. *Soft Matter* **2016**, *12*, 7457−7469.

(30) Qian, B.; Breuer, K. S. The Motion, Stability and Breakup of a Stretching Liquid Bridge with a Receding Contact Line. *J. Fluid Mech.* **2011**, *666*, 554−572.

DOI: 10.1021/acs.langmuir.9b00460
Langmuir 2019, 35, 7659−7671

(31) Gupta, M.; Gleason, K. K. Initiated Chemical Vapor Deposition of poly(1H,1H,2H,2H-Perfluorodecyl Acrylate) Thin Films. *Langmuir* **2006**, *22*, 10047−10052.
(32) Sojoudi, H.; Kim, S.; Zhao, H.; Annavarapu, R. K.; Mariappan, D.; Hart, A. J.; McKinley, G. H.; Gleason, K. K. Stable Wettability Control of Nanoporous Microstructures by iCVD Coating of Carbon Nanotubes. *ACS Appl. Mater. Interfaces* **2017**, *9*, 43287−43299.
(33) Rohsenow, W. M.; Hartnett, J. P.; Cho, Y. I. *Handbook of Heat Transfer Media*; McGraw-Hill, 1998.
(34) Jackson, G. W.; James, D. F. The Permeability of Fibrous Porous Media. *Can. J. Chem. Eng.* **1986**, *64*, 364−374.
(35) Zhao, H.; Jacob, C.; Stone, H. A.; Hart, A. J. Liquid Imbibition in Ceramic-Coated Carbon Nanotube Films. *Langmuir* **2016**, *32*, 12686−12692.
(36) McKinley, G. H. Visco-Elasto-Capillary Thinning and Break-Up of Complex Fluids. *Polymer* **2005**, *2005*, 1274−1277.
(37) de Gennes, P.-G.; Brochard-Wyart, F.; Quéré, D. *Capillarity and Wetting Phenomena—Drops, Bubbles, Pearls, Waves*; Springer Science & Business Media, 2002.
(38) Tanner, L. H. The Spreading of Silicone Oil on Horizontal Surfaces. *J. Phys. D Appl. Phys.* **1979**, *12*, 1473−1485.
(39) Mariappan, D.; Kim, S.; Hart, A. J. Plate to Roll Apparatus for Flexography Using Nanoporous Stamps. In Proceedings - ASPE 2016 Spring Topical Meeting: Precision Mechatronic System Design and Control, 2016.
(40) Ranfeld, C. Wet Etching of Printed Silver Layers Using an Etch Resist Structured by Flexography; Technische Universität Darmstadt, Ph.D. Thesis, 2015.
(41) Tamjid, E.; Guenther, B. H. Rheology and Colloidal Structure of Silver Nanoparticles Dispersed in Diethylene Glycol. *Powder Technol.* **2010**, *197*, 49−53.
(42) Kosmala, A.; Wright, R.; Zhang, Q.; Kirby, P. Synthesis of Silver Nano Particles and Fabrication of Aqueous Ag Inks for Inkjet Printing. *Mater. Chem. Phys.* **2011**, *129*, 1075−1080.
(43) De Kruif, C. G.; Van Iersel, E. M. F.; Vrij, A.; Russel, W. B. Hard Sphere Colloidal Dispersions: Viscosity as a Function of Shear Rate and Volume Fraction. *J. Chem. Phys.* **1985**, *83*, 4717−4725.
(44) Genovese, D. B. Shear Rheology of Hard-Sphere, Dispersed, and Aggregated Suspensions, and Filler-Matrix Composites. *Adv. Colloid Interface Sci.* **2012**, *171−172*, 1−16.
(45) Brady, J. F. The Rheological Behavior of Concentrated Colloidal Dispersions. *J. Chem. Phys.* **1993**, *99*, 567−581.
(46) Noguchi, Y.; Sekitani, T.; Yokota, T.; Someya, T. Direct Inkjet Printing of Silver Electrodes on Organic Semiconductors for Thin-Film Transistors with Top Contact Geometry. *Appl. Phys. Lett.* **2008**, *93*, No. 043303.
(47) Shiyong, L.; Ning, W.; Wencai, X.; Yong, L. Preparation and Rheological Behavior of Lead Free Silver Conducting Paste. *Mater. Chem. Phys.* **2008**, *111*, 20−23.
(48) Tseng, W. J.; Chen, C. N. Dispersion and Rheology of Nickel Nanoparticle Inks. *J. Mater. Sci.* **2006**, *41*, 1213−1219.
(49) Chen, C. N.; Huang, C. T.; Tseng, W. J.; Wei, M. H. Dispersion and Rheology of Surfactant-Mediated Silver Nanoparticle Suspensions. *Appl. Surf. Sci.* **2010**, *257*, 650−655.
(50) Sadowski, T. J.; Bird, R. B. Non-Newtonian Flow through Porous Media. I. Theoretical. *Trans. Soc. Rheol.* **1965**, *9*, 243−250.
(51) Mckinley, R. M.; Jahns, H.; Harris, W. W. Flow in Porous Media. *AIChE J. 12* 17 20. DOI: 10.1002/aic.690120106.

DOI: 10.1021/acs.langmuir.9b00460
Langmuir 2019, 35, 7659−7671